*Inorg. Chem.* **2009**, *48*, 2735−2747

Inorganic Chemistry
Article

# Mössbauer, Electron Paramagnetic Resonance, and Theoretical Studies of a Carbene-Based All-Ferrous $Fe_4S_4$ Cluster: Electronic Origin and Structural Identification of the Unique Spectroscopic Site

**Mrinmoy Chakrabarti,[†] Liang Deng,[‡] R. H. Holm,[*,‡] Eckard Münck,[*,†] and Emile L. Bominaar[*,†]**

*Department of Chemistry, Carnegie Mellon University, Pittsburgh, Pennsylvania 15213, and Department of Chemistry and Chemical Biology, Harvard University, Cambridge, Massachusetts 02138*

Received November 14, 2008

It is well established that the cysteinate-coordinated $[Fe_4S_4]$ cluster of the iron protein of nitrogenase from *Azotobacter vinelandii* (*Av*2) can attain the all-ferrous core oxidation state. Mössbauer and electron paramagnetic resonance (EPR) studies have shown that the all-ferrous cluster has a ground-state spin $S = 4$ and an effective 3:1 site symmetry in the spin structure and $^{57}Fe$ quadrupole interactions. Recently, Deng and Holm reported the synthesis of $[Fe_4S_4(Pr^i_2NHCMe_2)_4]$,[2] (**1**; $Pr^i_2NHCMe_2$ = 1,3-diisopropyl-4,5-dimethylimidazol-2-ylidene) and showed that the all-ferrous carbene-coordinated cluster is amenable to physicochemical studies. Mössbauer and EPR studies of **1**, reported here, reveal that the electronic structure of this complex is strikingly similar to that of the protein-bound cluster, suggesting that the ground-state spin and the 3:1 site ratio are consequences of spontaneous distortions of the cluster core. To gain insight into the origin of the peculiar ground state of the all-ferrous clusters in **1** and *Av*2, we have studied a theoretical model that is based on a Heisenberg−Dirac−van Vleck Hamiltonian whose exchange-coupling constants are a function of the Fe−Fe distances. By combining the exchange energies with the elastic deformation energies in the harmonic approximation, we obtain for a $T_2$ distortion a minimum with spin $S = 4$ and a $C_{3v}$ core structure in which one iron is unique and three irons are equivalent. This minimum has all of the spectroscopic and structural characteristics of the all-ferrous clusters of **1** and *Av*2. Our analysis maps the unique spectroscopic iron site to a specific site in the X-ray structure of the $[Fe_4S_4]^0$ core both in complex **1** and in *Av*2.

## 1. Introduction

The recent syntheses and structural determinations of $[Fe_4S_4(CN)_4]^{4-1}$ and the carbene-ligated cluster $[Fe_4S_4(Pr^i_2NHCMe_2)_4]$ (**1**)[2] complete the set of accessible cubane-type clusters having core oxidation levels $[Fe_4S_4]^z$ with charge $z$ ranging from 0 to 3+.[3] The cluster with $z = 0$ is of particular current interest because its all-ferrous core is isoelectronic with that present in the iron protein of *Azotobacter vinelandii* nitrogenase (called iron protein or *Av*2) when reduced with titanium(III) citrate.[4−6] Furthermore, the synthetic cluster cores are nearly isostructural with the $[Fe_4S_4]^0$ core of the fully reduced $[Fe_4S_4(S_{Cys})_4]$ cluster of the iron protein.[2,7] The carbene cluster, whose structure is depicted in Figure 1, is far more amenable to experimentation than the cyanide cluster because of its lesser tendency toward oxidation. The compound crystallizes in the monoclinic space group *Cc*; the cluster has the familiar cubane-type stereochemistry with no imposed symmetry and Fe−S bond lengths

* To whom correspondence should be addressed. E-mail: holm@chemistry.harvard.edu (R.H.H.), emunck@cmu.edu (E.M.), eb7g@andrew.cmu.edu (E.L.B.).
[†] Carnegie Mellon University.
[‡] Harvard University.

(1) Scott, T. A.; Berlinguette, C. P.; Holm, R. H.; Zhou, H.-C. *Proc. Natl. Acad. Sci. U.S.A.* **2005**, *102*, 9741–9744.
(2) Deng, L.; Holm, R. H. *J. Am. Chem. Soc.* **2008**, *130*, 9878–9886.
(3) Rao, P. V.; Holm, R. H. *Chem. Rev.* **2004**, *104*, 527–559.
(4) Angove, H. C.; Yoo, S. J.; Burgess, B. K.; Münck, E. *J. Am. Chem. Soc.* **1997**, *119*, 8730–8731.
(5) Angove, H. C.; Yoo, S. J.; Münck, E.; Burgess, B. K. *J. Biol. Chem.* **1998**, *273*, 26330–26337.
(6) Yoo, S. J.; Angove, H. C.; Burgess, B. K.; Hendrich, M. P.; Münck, E. *J. Am. Chem. Soc.* **1999**, *121*, 2534–2545.
(7) Strop, P.; Takahara, P. M.; Chiu, H.-J.; Angove, H. C.; Burgess, B. K.; Rees, D. C. *Biochemistry* **2001**, *40*, 651–656.

10.1021/ic802192w CCC: $40.75 
Published on Web 02/11/2009

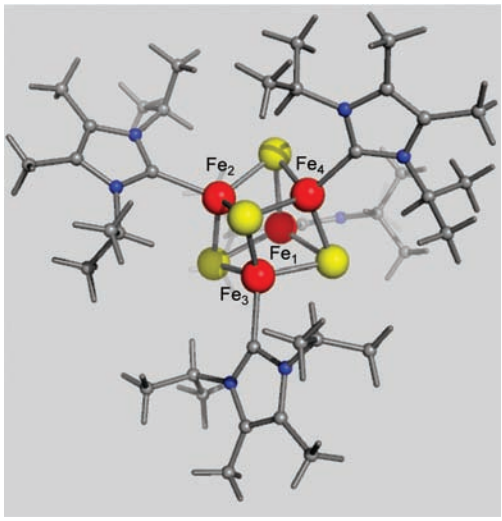


**Figure 1.** Structure of **1**.[2] Ranges and mean values (Å) of core distances: Fe−S 2.291(1)−2.338(1), 2.33(2); Fe−Fe 2.603(1)−2.764(1), 2.68(6). The irons labeled $Fe_1$, $Fe_2$, $Fe_3$, and $Fe_4$ correspond with the irons Fe(1), Fe(3), Fe(4), and Fe(2) of ref 2.

and other structural features consistent with the all-ferrous formulation.[2]

For the all-ferrous $[Fe_4S_4]^0$ cluster of *Av*2, a parallel-mode electron paramagnetic resonance (EPR) and Mössbauer spectroscopic study of the fully reduced native cluster demonstrated an effective 3:1 symmetry of iron sites that afford an $S = 4$ cluster ground state rather than an $S = 0$ state, as was expected for a symmetric cubane core.[6] This state is unique among protein-bound metal sites of any nuclearity and thus raises the issue of the effect of the protein structure and environment on stabilization of this state. The cluster is bound between two identical subunits of the iron protein and is potentially susceptible to the influence of both the protein structure and solvent. Further attention is directed toward native cluster properties by the report of an $[Fe_4S_4]^0$ cluster with a probable $S = 4$ state in the activator protein of a dehydratase[8] and the claim of an $S = 0$ all-ferrous cluster in the *A. vinelandii* iron protein when reduced with flavodoxin hydroquinone.[9] A detailed EPR and Mössbauer analysis of the carbene cluster, presented here, revealed that **1** has an $S = 4$ ground state like the *Av*2 $[Fe_4S_4]^0$ cluster. Moreover, the analysis indicates striking similarities between the $^{57}$Fe hyperfine parameters. Given that the two clusters have different external coordination, these findings suggested to us that the $S = 4$ ground state and the observed 3:1 site ratios reflect intrinsic properties of the cluster core rather than a perturbing influence of the environment. For small variations, $\Delta R_{i,j}$, the $Fe_iFe_j$ distances are linearly related to changes of the exchange-coupling constants, $\Delta J_{i,j}$. Using this correlation, we have investigated the energy surfaces of the combined action of elastic and exchange forces, finding that a global minimum is attained for a $T_2$ mode acting in the $S = 4$ manifold that yields a 3:1 pattern of magnetic hyperfine interactions, as observed experimentally.

(8) Hans, M.; Buckel, W.; Bill, E. *J. Biol. Inorg. Chem.* **2008**, *13*, 563–579.
(9) Lowery, T. J.; Wilson, P. E.; Zhang, B.; Bunker, J.; Harrison, R. G.; Nyborg, A. C.; Thiriot, D.; Watt, G. D. *Proc. Natl. Acad. Sci. U.S.A.* **2006**, *103*, 17131–17136.

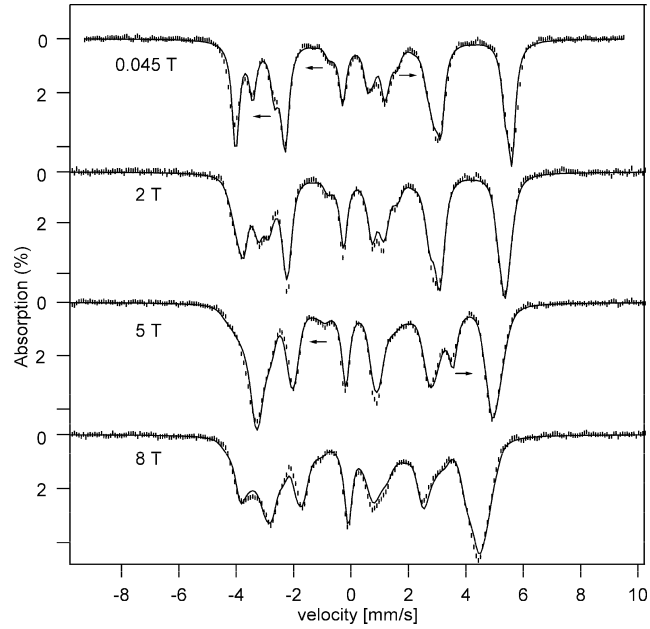


**Figure 2.** 4.2 K Mössbauer spectra of complex **1** recorded in the parallel applied magnetic fields indicated. The solid lines are simulations using the parameters quoted in Table 1. The arrows indicate the line displacements of the unique site upon increases in the magnetic field.

Elsewhere, we have provided a perspective of the carbene cluster in relation to the protein-bound all-ferrous cluster.[10]

## 2. Materials and Methods

$[Fe_4S_4(Pr^i_2NHCMe_2)_4]$ (**1**) was prepared as described.[2] To avoid orientation of the polycrystalline material in the Mössbauer spectrometer by the applied magnetic field, the sample was stirred into 0.3 mL Paratone-N oil before freezing. For EPR studies, solid **1** was dissolved in toluene to yield a 7.9 mM solution. Mössbauer spectra were collected with constant-acceleration spectrometers, using two cryostats that allowed studies at 4.2 K in applied fields up to 8.0 T. Isomer shifts are quoted relative to iron metal at 298 K. Spectra were analyzed with the WMOSS software package (Web Research Co., Edina, MN). X-band EPR spectra were recorded on a Bruker EMX spectrometer, using a Hewlett-Packard 5352B microwave-frequency counter, an ER4102 ST cavity, and an Oxford Instruments ESR 900 cryostat. Spectra were analyzed with the program *SpinCount* written by M. P. Hendrich at Carnegie Mellon University.

## 3. Results

**3.1. Mössbauer Studies of Polycrystalline 1.** We have studied a polycrystalline sample of all-ferrous **1** with Mössbauer spectroscopy between 2 and 140 K in applied magnetic fields up to 8.0 T. An EPR study of the polycrystalline material was unsuccessful for two reasons. First, the observed resonances were very broad and, second, at low temperatures the uniaxial electronic system led to partial alignment of crystallites by the applied field. We therefore decided to study the EPR spectra of **1** in toluene, a glassing solvent that produced well-resolved spectra. We discuss the Mössbauer spectra first, using from EPR the information that **1** has an $S = 4$ ground state with zero-field-splitting (ZFS) parameters $D = -1.9$ cm$^{-1}$ and $E/D \approx 0.07$. Figure 2 shows a series of 4.2 K spectra, recorded in applied field as

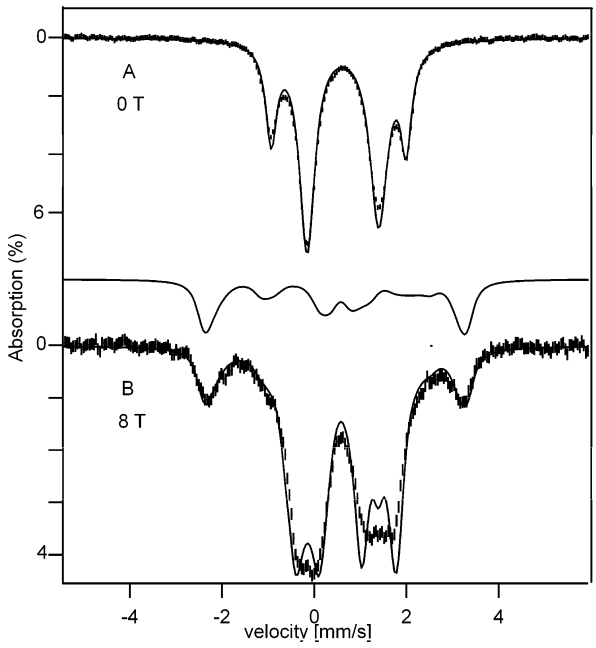


**Figure 3.** 100 K Mössbauer spectra of complex **1** recorded in zero field (A) and an 8.0 T field applied parallel to the $\gamma$ beam (B). The solid lines are simulations using the parameters quoted in Table 1. The solid curve above the spectrum in B is the contribution of site 4.

indicated, and Figure 3 features a zero field and an 8.0 T spectrum, both recorded at 100 K.

The Mössbauer and EPR spectra were analyzed with the $S = 4$ spin Hamiltonian

$$\hat{\mathcal{H}} = \hat{\mathcal{H}}_e + \hat{\mathcal{H}}_{hf} \quad (1)$$

$$\hat{\mathcal{H}}_e = D[\hat{S}_z^2 - 20/3 + (E/D)(\hat{S}_x^2 - \hat{S}_y^2)] + \beta \hat{\mathbf{S}} \cdot \mathbf{g} \cdot \mathbf{B} \quad (2)$$

$$\hat{\mathcal{H}}_{hf} = \sum_{i=1,4} \{\hat{\mathbf{S}}_i \cdot \mathbf{A}_i \cdot \hat{\mathbf{I}}_i - g_n \beta_n \mathbf{B} \cdot \hat{\mathbf{I}}_i + \hat{\mathcal{H}}_{Q,i}\} \quad (3)$$

$$\hat{\mathcal{H}}_{Q,i} = \frac{1}{12} eQV_{i,\zeta\zeta}[3\hat{I}_{i,\zeta}^2 - I(I+1) + \eta_i(\hat{I}_{i,\xi}^2 - \hat{I}_{i,\eta}^2)] \quad (4)$$

where all of the parameters have their conventional meaning. In eq 2, we have written the ZFS term in its principal axis system $\{x, y, z\}$, which we will use as our frame of reference. For our Mössbauer analysis, we have used an isotropic **g** tensor and set $g = 2$ ($g_z = 2.02$ from EPR; see below). Complex **1** has $C_1$ symmetry, implying that all tensors in eqs 1−4 may have different principal axis systems. In the following, we discuss the main features of the Mössbauer spectra and indicate how the various parameters can be extracted.

The 4.2 K spectra of the four subsites of **1** exhibit simple six-line patterns. The intensities of the absorption lines did not depend on whether the 45 mT applied field was oriented parallel or perpendicular to the observed $\gamma$ radiation. This observation implies that the electronic ground state is magnetically uniaxial; i.e., the expectation value of the electron spin is nonzero only in one direction, implying that the axial parameter of the ZFS tensor **D** is negative, $D < 0$. As shown in Figure 4A,B, the same Mössbauer spectrum was observed for $B = 0$ and 45 mT. In general, the electronic levels of systems with integer electronic spins are singlets, unless degeneracies occur as a consequence of the symmetry. In the absence of an applied magnetic field, an electronic singlet does not yield a Mössbauer spectrum exhibiting magnetic hyperfine structure, in contrast to what is observed for **1**. It follows that the spin ground state of **1** must be degenerate. It was shown in ref 11 that a $^{57}$Fe magnetic hyperfine structure is observed for $B = 0$ if the splitting $\Delta$ of the $M_S = \pm S$ levels (here $M_S = \pm 4$) fulfills the condition $\Delta < |A_{i,z}|$, where $A_{i,z}$ is the component of the magnetic hyperfine tensor of site $i$ along the $z$ axis of the ZFS tensor. Typically, $A$ values of $[Fe_4S_4]$ clusters are on the order of 10 MHz, implying that $\Delta$ has to be smaller than $10^{-3}$ cm$^{-1}$. For an $S = 4$ system, the splitting of the $M_S = \pm 4$ doublet is given by $\Delta = 2.2\ D(E/D)^4$ and thus the condition $\Delta < 10^{-3}$ cm$^{-1}$ may often be fulfilled for $E/D \leq 0.1$ as long as $D$ is only a few wavenumbers.

For small $D$ values, the $M_S = \pm 4$ multiplet is readily magnetized along the $z$ axis, yielding for $\beta B/|D| \ll 1$ a large disparity in the components of the spin expectation values of the ground state, $\langle S_x \rangle = \langle S_y \rangle \approx 0$ and $\langle S_z \rangle = -4$ (see Figure S1 in the Supporting Information). The magnetic hyperfine field at the $^{57}$Fe nucleus can be written as[12]

$$\mathbf{B}_{int,i} = -\langle \hat{\mathbf{S}} \rangle \cdot \mathbf{A}_i / g_n \beta_n \quad (5)$$

For small applied fields, $\mathbf{B}_{int,i}$ assumes a fixed orientation relative to the electric field gradient (EFG) tensor, described by the polar angles $\theta_i$ and $\varphi_i$. The low-field spectra then depend on $\Delta E_{Q,i}$, $\eta_i$, $\mathbf{B}_{int,i}$, $\theta_i$, and $\varphi_i$. It has been shown that there exists an infinite manifold of $\{\eta_i, \theta_i, \varphi_i\}$ values that yield identical Mössbauer spectra (this so-called ambiguity problem has been described in the literature[13,14]). In strong applied magnetic fields, where $\langle S_x \rangle$ and $\langle S_y \rangle$ compete with $\langle S_z \rangle$, each set $\{\eta_i, \theta_i, \varphi_i\}$ may yield unique spectra. Thus, a parameter set that fits at low field may fail to do so at high field. The low-temperature spectra of Figure 2 depend on as many as 50 parameters, namely, $D$ and $E/D$, together with four sets of $\{A_{x'}, A_{y'}, A_{z'}, \Delta E_Q, \eta, \delta, \alpha_A, \beta_A, \gamma_A, \alpha_{EFG}, \beta_{EFG}, \gamma_{EFG}\}_i$. Here $\{x', y', z'\}$ denotes the principal axis system of the **A** tensor, and $\alpha_A$, $\beta_A$, and $\gamma_A$ are the Euler angles that rotate $\{x', y', z'\}$ into the principal axis system $\{x, y, z\}$ of the ZFS tensor, our system of reference; $\alpha_{EFG}$, $\beta_{EFG}$, and $\gamma_{EFG}$ rotate the EFG tensor into $\{x, y, z\}$. All rotations are those used in WMOSS; note that WMOSS uses the "$x$" convention for the Euler angles. $D$, $E/D$, $\Delta E_Q$, and $\delta$ are reasonably well determined from considerations given below. In the following, we describe how the various parameters were determined.

At 4.2 K, the electronic spin of **1** relaxes slowly on the time scale of Mössbauer spectroscopy (ca. 10 MHz). As the temperature is raised above 4.2 K, the absorption features

(10) Münck, E.; Bominaar, E. L. *Science* **2008**, *321*, 1452–1453.
(11) Surerus, K. K.; Hendrich, M. P.; Christie, P. D.; Rottgardt, D.; Orme-Johnson, W. J.; Münck, E. *J. Am. Chem. Soc.* **1992**, *114*, 8579–8590.
(12) Münck, E.; Surerus, K. K.; Hendrich, M. P. *Methods Enzymol.* **1993**, *227*, 463–479.
(13) Zimmermann, R.; Münck, E.; Brill, W. J.; Shah, V. K.; Henzl, M. T.; Rawlings, J.; Orme-Johmson, W. H. *Biochim. Biophys. Acta* **1978**, *537*, 185–207.
(14) Dabrowski, L.; Piekoszewski, J.; Suwalski, J. *Nucl. Instrum. Methods* **1971**, *91*, 93–95.

**Table 1.** Mössbauer Parameters for the $S = 4$ State of Complex **1**[a] and the $[Fe_4S_4]^0$ State of $A\nu2$[b]

| site[c] | | $\delta$[d] (mm/s) | $\Delta E_Q$[d] (mm/s) | $\eta$ | $\alpha_{efg}$ (deg) | $\beta_{efg}$ (deg) | $\gamma_{efg}$ (deg) | $A_x$ (kG) | $A_y$ (kG) | $A_z$ (kG) | $\alpha_A$ (deg) | $\beta_A$ (deg) | $\gamma_A$ (deg) |
|---|---|---|---|---|---|---|---|---|---|---|---|---|---|
| 1[e] | **1** | 0.61 | −1.6 | 0 | 0 | 90 | 0 | −74 | −65 | −66.5 | 0 | 0 | 0 |
| | $A\nu2$ | 0.68 | −1.24 | 0.54 | 0 | 90 | 90 | −98 | −79 | −70 | 0 | 0 | 0 |
| 2 and 3 | **1** | 0.62 | −1.5 | 0.1 | 0 | 105 | 0 | −98 | −57 | −70 | 0 | 15 | 0 |
| 2 | $A\nu2$ | 0.68 | −1.72 | 0 | 0 | 56.6 | 4.6 | −86 | −76 | −81 | 0 | 0 | 0 |
| 3 | $A\nu2$ | 0.68 | −1.48 | 0 | 0 | 92.3 | 0 | −100 | −73 | −73 | 0 | 0 | 0 |
| 4[e] | **1** | 0.54 | 2.96 | 0.59 | 0 | 90 | 90 | 7.7 | 57 | 29 | 0 | 0 | 0 |
| | $A\nu2$ | 0.68 | 3.08 | 0.59 | 90 | 90 | 52.8 | 22 | 25 | 63 | 0 | 150 | 0 |

[a] $D = -1.9$ cm$^{-1}$ and $E/D = 0.07$ were used for the simulation. [b] $D = -0.75$ cm$^{-1}$ and $E/D = 0.33$ were used for the simulation. [c] The iron sites of $A\nu2$ labeled 1, 2, 3, and 4 correspond with the sites 4, 2, 3, and 1 in ref 6, respectively. [d] At 4.2 K. [e] For sites 1 and 4 of $A\nu2$, the coordinate frame $\{x', y', z'\}$ was adopted to fulfill the convention $0 \le \eta \le 1$.

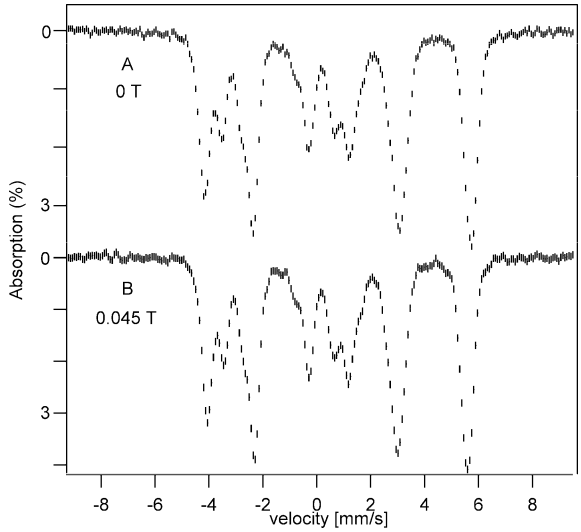


**Figure 4.** 4.2 K Mössbauer spectra of complex **1** recorded in zero field (A) and an 0.045 T field applied parallel to the $\gamma$ beam (B).

broaden in a way characteristic of intermediate relaxation rates. At $T = 100$ K, the spin system is nearly in the fast relaxation limit, and consequently quadrupole doublets are observed. Figure 3A shows a zero-field spectrum recorded at 100 K. This spectrum exhibits two doublets in a 3:1 intensity ratio, similar to what has been reported for the all-ferrous $A\nu2$ cluster. The most noteworthy differences between the two clusters are the smaller isomer shifts of **1**, namely, $\delta = 0.62$ mm/s for sites 1−3 and $\delta = 0.54$ mm/s for site 4 ($\Delta E_{Q,4} = 2.92$ mm/s at 100 K). The quadrupole splittings of sites 1−3 are quite similar and are not resolved, $\Delta E_Q \approx 1.5-1.6$ mm/s but are distinctly smaller than that of site 4. The spectrum in Figure 3B was recorded in a parallel field of 8.0 T. Matching the splittings of the theoretical curves with the experimental data requires $B_{int,1-3} < 0$ and $B_{int,4} > 0$, suggesting that the local $S = 2$ spins of the four high-spin ferrous sites are coupled similarly to those in the protein-bound cluster; namely, the spins of sites 1−3 are aligned parallel to the cluster spin and that of site 4 is antiparallel.

Analysis of the spectra of Figure 2 shows that at 4.2 K only the $M_S = \pm4$ doublet is populated; for $D = -1.9$ cm$^{-1}$ (see below), the $M_S = \pm3$ quasi-doublet is at energy $E/k_B \approx 19$ K. The quasi-degenerate ground state has $g_{eff} = 16$, and the system is essentially in the $M_S = -4$ level for $B > 1$ T. Inspection of the applied field spectra in Figure 2 shows that most absorption lines move toward the center with increasing applied fields, implying that they belong to sites with negative $B_{int}$, while some, namely, those belonging to site 4 (arrows),

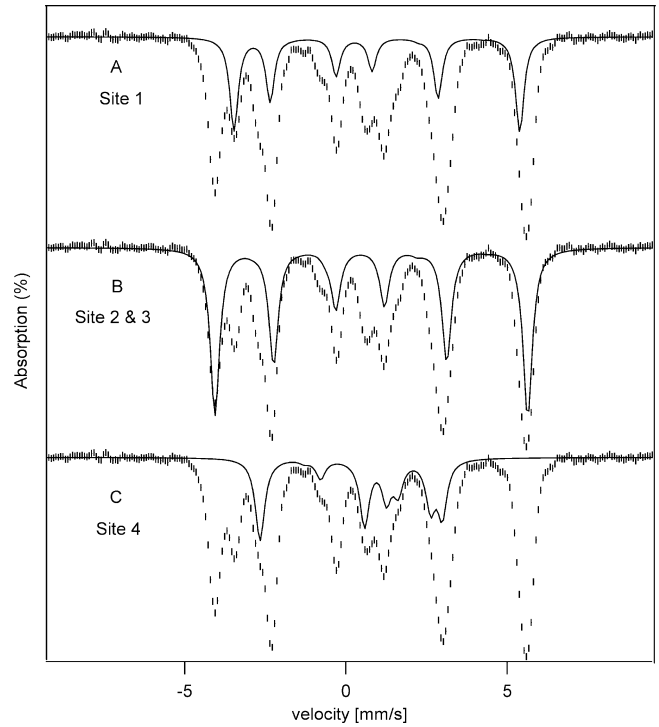


**Figure 5.** 4.2 K Mössbauer spectrum of complex **1** recorded in a 0.045 T magnetic field applied parallel to the $\gamma$ beam (same as that in Figure 2). Solid lines drawn through the data show the contributions of site 1 (A), sites 2 and 3 (B), and site 4 (C).

move outward and have $B_{int} > 0$. From the 100 K data, it follows that the outward moving lines in Figure 3B belong to site 4. Outward and inward moving lines must belong to different iron sites. Figure 5 shows the 45 mT Mössbauer spectrum of Figure 4B together with the theoretical spectra of the subsites (the sum of these spectra is shown in Figure 2). We believe that this decomposition is essentially correct. In searching for decomposition of the spectra, we observed that two sites, 2 and 3, gave essentially identical spectra, and thus we have treated them, henceforth, as one site accounting for 50% of the spectral intensity.

We mentioned above that the parameter set obtained at low applied fields is not unique. For **1**, one has to apply fields larger than 5 T to induce sizable expectation values $\langle S_x \rangle$ and $\langle S_y \rangle$. We have used the 8.0 T spectrum of Figure 2 for reduction of the ambiguities of the low-field spectra, using the following procedure. Starting with the parameters obtained at low field, we have least-squares-fitted all spectra of Figure 2 as a group, allowing all parameters except $D$, $E/D$, $\Delta E_Q$, and $\delta$ to vary freely. This procedure produced a set of parameters (Table 1) that represented the set of spectra

quite well. Interestingly, for this parameter set, the **A** tensors of sites 1 and 4 were found to be aligned with $\{x, y, z\}$, implying that, at low field, $\mathbf{B}_{int,1}$ and $\mathbf{B}_{int,4}$ are along the easy axis of magnetization, the $z$ axis of eq 2. For sites 2 and 3, the $z'$ axis of $\mathbf{A}_{2,3}$ is tilted by $\beta_A = 15°$ relative to the $z$ axis.

We mentioned above that, at low field, there exists an infinite manifold of $\{\eta_i, \theta_i, \varphi_i\}$ values yielding the same Mössbauer spectrum (for sites 1 and 4 and the polar angles $\theta$ and $\varphi$ correspond to $\beta_{EFG}$ and $\gamma_{EFG}$; for sites 2 and 3, they relate the EFG tensor to $\mathbf{B}_{int,2,3}$). However, the ranges of these three parameters can often be narrowed considerably. In order to explore the allowed ranges, we have used the following procedure: We have taken the simulated spectra of Figure 2 and added random noise to treat them in WMOSS as an "experimental" spectrum. We have least-squares-fitted these "experimental" spectra by fixing one of the three parameters and exploring whether a good fit could be obtained. The ranges of allowed $\{\eta_i, \theta_i, \varphi_i\}$ are indicated in Table S1 in the Supporting Information.

The ZFS parameters $D$ and $E/D$ differ substantially for the all-ferrous $A\upsilon 2$ cluster and the synthetic model **1**. The former has $D = -0.7$ cm$^{-1}$ and $E/D = 0.33$, whereas **1** has $D = -1.9$ cm$^{-1}$ and $E/D = 0.07$. The larger $D$ value of **1** implies that the electronic levels are less mixed at 8.0 T, rendering the Mössbauer spectra less sensitive to components of the magnetic hyperfine tensors perpendicular to the electronic $z$ axis. On the other hand, the spectra of the $A\upsilon 2$ cluster are poorly resolved at high fields, a fact that severely limits the data analysis.

Using the parameters of Table 1 and assuming that the electronic system relaxes fast on the Mössbauer time scale, we have generated the theoretical curves of Figure 3B. Site 4 is well represented by these simulations. The simulation for sites 1−3 gives the right splitting but not quite the correct shape probably because for these sites the spin system is only approximately near the fast fluctuation limit, a conclusion supported by the observation that the high-energy lines of doublets 1−3 are broadened in the zero-field spectrum of Figure 3A. We did not record an 8.0 T spectrum above 100 K because $\Delta E_{Q,4}$ decreased rapidly above 100 K, leading to a lack in resolution.

Finally, because the electron spin is in the slow fluctuation limit at 4.2 K, each populated electronic level will contribute its own Mössbauer spectrum. Our spectral simulations give no evidence for the presence of spectral components originating from the $M_S = \pm 3$ levels, yielding $|D| > 1.6$ cm$^{-1}$, consistent with the EPR data obtained in toluene, $D = -1.9$ cm$^{-1}$.

**3.2. EPR Studies.** We have studied parallel-mode X-band EPR spectra of **1** dissolved in toluene between 2 and 50 K. Two spectra are shown in Figure 6. The 8 K spectrum exhibits a resonance near $g_{eff} = 12$, which originates from an excited state, as the intensity of this feature declines upon lowering the temperature and nearly disappears at 2 K. At 2 K a sharp resonance, belonging to the ground state, is observed at $g_{eff} = 16.08$. We assign these resonances to an $S = 4$ system with $D < 0$. Thus, the $g_{eff} = 16.08$ feature originates from the $M_S = \pm 4$ ground-state doublet, whereas

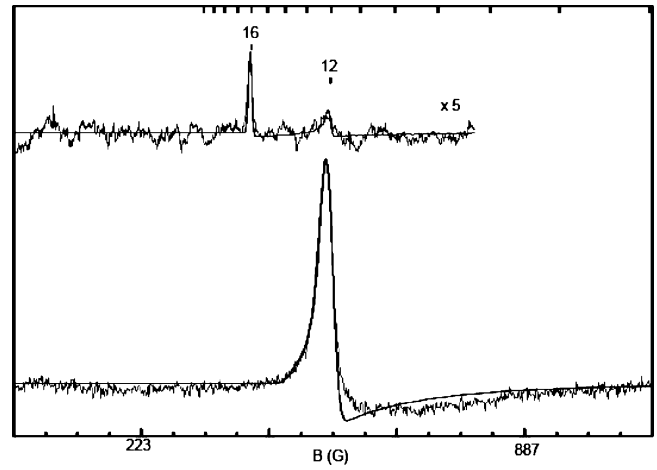


**Figure 6.** X-band parallel-mode EPR spectra of complex **1** recorded at 2 K (top) and 8 K (bottom). Conditions: frequency 9.27 GHz; microwave power 2 mW (top) and 0.2 mW (bottom); modulation 0.3 mT (top) and 1 mT (bottom). The solid lines drawn through the data are simulations, using *SpinCount*, for an $S = 4$ system with $D = -1.9$ cm$^{-1}$, $E/D = 0.07$, $\sigma_{E/D} = 0.03$, $g_x = g_y = 2$, and $g_z = 2.015$.

the $g_{eff} = 12$ feature reflects a transition between the $M_S = \pm 3$ levels. As discussed for the $S = 4$ system of the all-ferrous cluster of the nitrogenase iron protein,[6] the energy separation for each quasi-doublet is predicted from eq 2 to be

$$\delta E = [\Delta^2 + (2\beta g_{eff} B_z)^2]^{1/2} \quad (6)$$

where $\Delta$ is the ZFS of the doublet. From the Mössbauer analysis of **1**, we know that $\Delta_g = 2.2|D|(E/D)^4 < 10^{-3}$ cm$^{-1}$ for the $M_S = \pm 4$ ground-state doublet, and thus $\delta E = 2\beta g_{eff} B_z$. For this quasi-doublet, $g_{eff} = 2Sg_z$, yielding $g_z = 2.015$ ($g_z$ is defined in eq 2). With the Mössbauer estimate $D \approx -2$ cm$^{-1}$, it follows that $E/D < 0.12$.

The solid lines in Figure 6 are spectral simulations performed with *SpinCount*, using the parameters quoted in the caption. The line shape of the $g_{eff} \approx 12$ feature was simulated by assuming that $E/D$ has a Gaussian distribution with $(E/D)_{avg} = 0.07$ and $\sigma_{E/D} = 0.03$. Although the spectral shape is reasonably well represented by the simulations, there are small discrepancies, indicating perhaps that the assumption of a Gaussian distribution for $E/D$ is only approximately correct.

We have studied the $g_{eff} = 12$ resonance over a wide range of temperatures. This feature maximizes near $T = 12-14$ K and broadens steadily as the temperature is increased. By using the amplitude of the $g_{eff} = 12$ feature between 10 and 25 K and fitting with variable-packet line width (1−2 mT), we obtained $D = -1.9 \pm 0.3$ cm$^{-1}$. We also found that we get a good estimate for $D$ and $E/D$ by noting that the intensity of the $g_{eff} = 12$ resonance is proportional to $D(E/D)$.[6] Thus, for $E/D = 0.07$ and $D = 1.9$ cm$^{-1}$, we obtain a good amplitude match by assuming a concentration of 7.5 mM of **1**, which compares well with the actual concentration of 7.9 mM.

**3.3. Comparison of Mössbauer Spectra of Complex 1 and Those of All-Ferrous $A\upsilon 2$.** There are interesting spectroscopic similarities between the Mössbauer spectra of the all-ferrous cluster of $A\upsilon 2$ and those of the carbene-

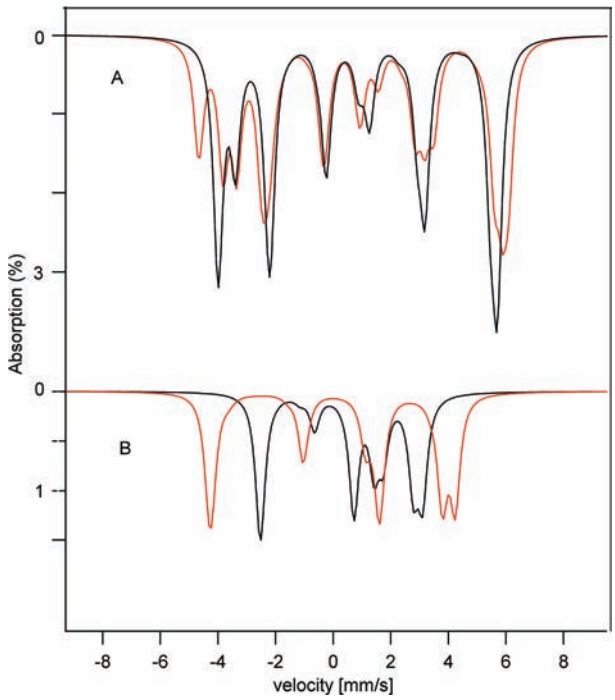


**Figure 7.** (A) Simulated Mössbauer spectra (sum of sites 1−3) at 1.5 K, 0.045 T for the $A\upsilon 2$ protein (red line), and at 4.2 K, 0.045 T for complex **1** (black line). (B) Simulated Mössbauer spectra of site 4 at 1.5 K, 0.045 T for the $A\upsilon 2$ protein (red line), and at 4.2 K, 0.045 T for complex **1** (black line).

coordinated model complex (Figure 7). Both systems have a ground state with cluster spin $S = 4$. It is instructive to compare the 4.2 K Mössbauer spectra of complex **1** with the 1.5 K spectra of the protein observed in weak applied magnetic fields. Given that $D$ is larger in **1**, we can use for this complex a higher temperature without noticeably populating excited doublets. For this purpose, we present the theoretical spectra. Not only do these represent the experimental data quite well, they can easily be manipulated to facilitate comparison of the relevant features. Thus, the lower isomer shifts of **1** compared to $A\upsilon 2$, by ~0.08 mm/s, are consistent with the poorer electron donation of the terminal carbene ligands to the 3d orbitals of the iron sites compared to the cysteine sulfurs. All iron sites of the $A\upsilon 2$ cluster have $\delta = 0.68$ mm/s at 4.2 K, and therefore we have set, for the sake of comparison, the isomeric shift for each iron site of **1** equal to 0.68 mm/s. There is a subtle point that should be mentioned: because $\Delta_g < 10^{-3}$ cm$^{-1}$ for **1** and $30 \times 10^{-3}$ cm$^{-1}$ for the $A\upsilon 2$ cluster,[6] one needs a field of at least $B = 0.045$ T to fulfill the condition $g_{\text{eff}}\beta B \gg \Delta_g$ to obtain fully developed magnetic spectra in both of the systems (Figure 7). Thus, we have simulated the spectra of Figure 7 for $B = 0.045$ T.

Figure 7A shows that the spectra of sites 1−3 are strikingly similar, the major difference being that the spectral sites 2 and 3 of the carbene model are indistinguishable whereas those of the $A\upsilon 2$ cluster are slightly nonequivalent. In contrast, the spectra of site 4 exhibit quite different magnetic splittings (Figure 7B). We wondered whether the $A\upsilon 2$ spectra would admit a solution with substantially different $A$ values for site 4. However, reexamination of the spectra confirmed that the assignments of Yoo et al.[6] are essentially correct. It should be noted that the principal values of $\mathbf{A}_4$ do not differ by much in the two systems; however, the tensors are oriented differently relative to the easy axis of magnetization, $z$.

**Table 2.** Spin Quantum Numbers, Numbers of Spin Multiplets, Spin-State Energies, and Relative Energies for an All-Ferrous Cluster with Six Equal Exchange-Coupling Constants between the Four Irons

| $S$ | no. of multiplets | $E°(S)/J°$ | $[E°(S) - E°(0)]/J°$ |
|---|---|---|---|
| 0 | 5 | −12 | 0 |
| 1 | 12 | −11 | 1 |
| 2 | 16 | −9 | 3 |
| 3 | 17 | −6 | 6 |
| 4 | 15 | −2 | 10 |
| 5 | 10 | 3 | 15 |
| 6 | 6 | 9 | 21 |
| 7 | 3 | 16 | 28 |
| 8 | 1 | 24 | 36 |

## 4. Theoretical Model for the All-Ferrous Cluster

**4.1. Formulation of Model.** The following analysis rests on the assumption that the exchange interactions between the paramagnetic iron sites of the all-ferrous cluster are described by the Heisenberg− Dirac−van Vleck Hamiltonian

$$\hat{\mathcal{H}} = \sum_{i=1}^{3}\sum_{j=i+1}^{4} J_{ij}\hat{\mathbf{S}}_i \cdot \hat{\mathbf{S}}_j \tag{7}$$

where the $\hat{\mathbf{S}}_i$ are the spin operators of the high-spin ferrous iron sites of the cluster ($S_i = 2$, $i = 1-4$) and $J_{ij}$ are the exchange-coupling constants between them. In general, including the case that the exchange-coupling constants have different values, the eigenstates of eq 7 are eigenfunctions of the square of the total spin operator, $\hat{\mathbf{S}}^2$, with $\hat{\mathbf{S}} = \sum_{i=1}^{4}\hat{\mathbf{S}}_i$. For $T_d$ symmetry of the cluster, all exchange-coupling constants are equal, $J_{ij} = J°$, and the energies for each value of the total spin are degenerate and given by (see Table 2)

$$E°(S) = J°\left\{\frac{1}{2}S(S+1) - 12\right\} \tag{8}$$

Exchange-coupling constants are known to be sensitive functions of structure, in particular of bridging bond angles and associated metal−metal distances, $J_{ij} = J(R_{ij})$ ($\theta_{ij}$ and $R_{ij}$ in Figure 8).[15] Small variations in the distances, $R_{ij} = R° + \Delta R_{ij}$, yield linear changes in the exchange-coupling constants

$$J_{ij} \approx J° + \frac{\mathrm{d}J}{\mathrm{d}R}\Delta R_{ij} = J° + \Delta J_{ij} \tag{9}$$

where $J° = J(R°)$ is the exchange-coupling constant for the undistorted cluster. The elastic deformation energies can be expressed as

$$E_{\text{elastic}} = K\sum_{i=1}^{3}\sum_{j=i+1}^{4}\Delta R_{ij}^{\,2} = k\sum_{i=1}^{3}\sum_{j=i+1}^{4}\Delta J_{ij}^{\,2} \tag{10}$$

$K$ is a force constant for stretching the Fe−Fe distances. These distances stand in a linear relationship with the

(15) Kahn, O. *Molecular Magnetism*; Verlag-Chemie: New York, 1993. *Magneto-Structural Correlations in Exchange Coupled Systems*; Willett, R. D. Gatteschi, D., Kahn O., Eds.; NATO Advances Study Institute Series C: Mathematical and Physical Sciences; Reidel Publishing: Dordrecht, The Netherlands, 1985; Vol. 140.

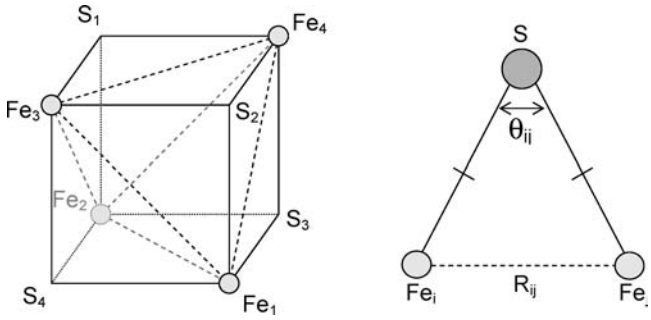


**Figure 8.** (left) Schematic representation of the core of an Fe−S cluster, showing the labeling of the core atoms and the six Fe−Fe distances considered in the theoretical model. The sulfur atoms are located outside the cube spanned by the irons. (right) One of the Fe−S−Fe bridges in the cluster, showing an Fe−Fe distance and the associated bond angle.

variations in the exchange-coupling constant (eq 9), allowing us to express the elastic energy as in the third term of eq 10, using the pseudo force constant $k$.

$$k = \left(\frac{\mathrm{d}J}{\mathrm{d}R}\right)^{-2} K \tag{11}$$

Combining the exchange and elastic energies yields the Hamiltonian

$$\hat{\mathscr{H}} = \sum_{i=1}^{3} \sum_{j=i+1}^{4} \{(J^\circ + \Delta J_{ij})\hat{\mathbf{S}}_i \cdot \hat{\mathbf{S}}_j + k\Delta J_{ij}^{\,2}\} \tag{12a}$$

By introduction of the dimensionless parameters $\delta J_{ij} = \Delta J_{ij}/J^\circ$ and $\kappa = J^\circ k$, eq 12a can also be written as

$$\hat{\mathscr{H}} = J^\circ \sum_{i=1}^{3} \sum_{j=i+1}^{4} \{(1 + \delta J_{ij})\hat{\mathbf{S}}_i \cdot \hat{\mathbf{S}}_j + \kappa \delta J_{ij}^{\,2}\} \tag{12b}$$

The space spanned by the six variables $\delta J_{ij}$ can be decomposed into irreducible representations of the $T_d$ group, $A_1$ $\{a_1\}$ + E $\{e_\varepsilon, e_\theta\}$ + $T_2$ $\{t_1, t_2, t_3\}$. The basis vectors (in curly brackets) are given by the combinations

$$a_1 = [\delta J_{12} + \delta J_{34} + \delta J_{13} + \delta J_{24} + \delta J_{14} + \delta J_{23}]/\sqrt{6} \tag{13}$$

$$e_\varepsilon = [\delta J_{13} + \delta J_{24} - (\delta J_{14} + \delta J_{23})]/2 \tag{14a}$$

$$e_\theta = [2(\delta J_{12} + \delta J_{34}) - (\delta J_{13} + \delta J_{24} + \delta J_{14} + \delta J_{23})]/\sqrt{12} \tag{14b}$$

$$t_1 = [\delta J_{12} - \delta J_{34}]/\sqrt{2} \tag{15a}$$

$$t_2 = [\delta J_{13} - \delta J_{24}]/\sqrt{2} \tag{15b}$$

$$t_3 = [\delta J_{14} - \delta J_{23}]/\sqrt{2} \tag{15c}$$

The symmetry-breaking $T_2$ and E distortions are illustrated in Figure 9. We have determined the eigenvalues and corresponding eigenstates of eq 12b by numerical diagonalization and studied the lowest of the resulting energies as a function of the distortion coordinates for each allowed value $S$. The resulting potential energy surfaces for $S = 0$ in the E space and $S = 4$ in a two-dimensional section of the $T_2$ space are shown in Figure 10. Both of the E and $T_2$ modes are Jahn−Teller active in the $S = 1, 2,..., 7$ spaces. The space of maximum spin, $S = 8$, is inactive with respect to both the E and $T_2$ distortions, and the $S = 0$ space exhibits only E distortions. The minima for a given distortion symmetry are degenerate, 3-fold for E and 4-fold for $T_2$. Depending on their relative energies, these minima are either global or local minima of the potential energy surfaces defined in the six-dimensional distortion space. The minima correspond to core structures with symmetry lower than $T_d$. The symmetry breaking is spontaneous and results from first-order interactions between the degenerate states of given spin $S$ that are generated by changes in the exchange parameters induced by geometrical distortions of the cluster. In the following two sections, we discuss the structures, spin states, and energies at the minima of the potential energy surfaces for $T_2$ and E.

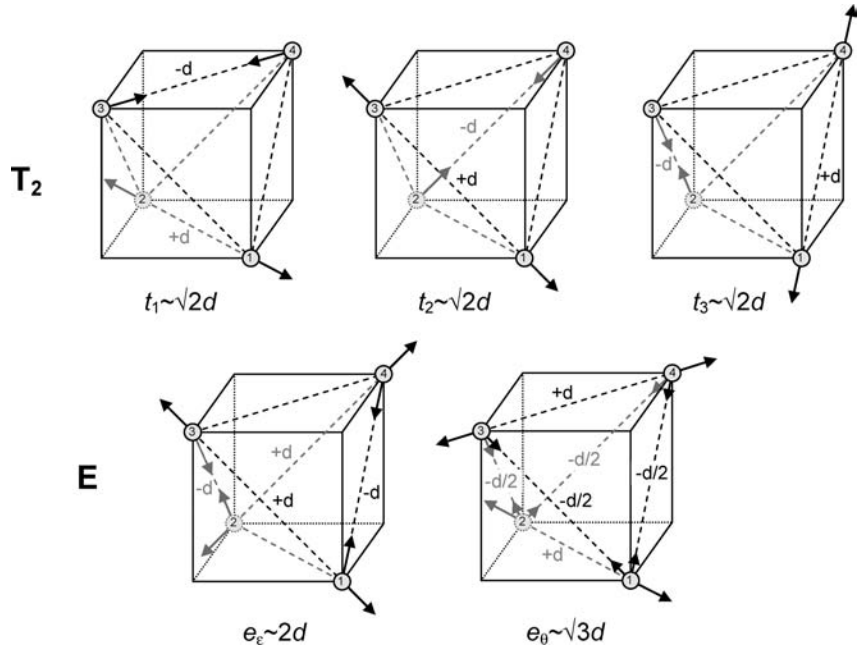


**Figure 9.** Symmetrized distortion coordinates of $T_2$ and E symmetry, defined in eqs 14a,b and 15a,b,c, describing the changes in the Fe−Fe distances. The iron positions have been superimposed on a cube for visual guidance.

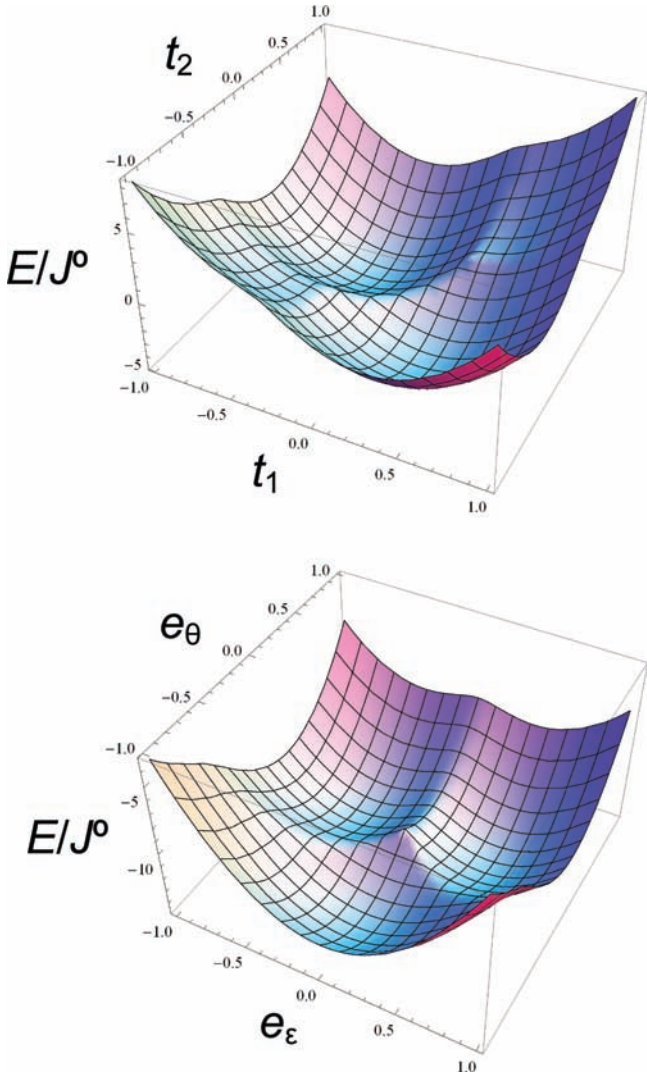


**Figure 10.** (top) Two-dimensional section at $t_3 = -13\sqrt{2}/60 \approx 0.3064$ of the potential energy surface of the cluster for $S = 4$ and $\kappa_T = 10$ defined on the three-dimensional $T_2$ space, containing two of the four degenerate minima (see also Figure 11, left). (bottom) Potential energy surface of the cluster for $S = 0$ and $\kappa_E = 10$ defined on the two-dimensional E space, showing three degenerate minima (see also Figure 11, right).

**4.2. $T_2$ Distortions.** The four degenerate minima of the potential energy surface for the ground state in the $T_2$ space are located at the vertices of an equilateral tetrahedron (Figure 11, left). The symmetry of the cluster at the minima is $C_{3v}$. The 3-fold axis runs through one of the four irons (called here the unique site); the remaining three sites are interchangeable by the $C_3$ operation. The six exchange-coupling constants at the $T_2$ minima are partitioned into two sets of three. For example, in the minimum for which $Fe_4$ is the unique site, there are two exchange-coupling constants, namely, $J = J_{14} = J_{24} = J_{34}$ and $J' = J_{12} = J_{13} = J_{23}$ with $J' < J$. The latter three coupling constants provide strong antiferromagnetic interactions between the unique site and the other three sites, which among themselves are coupled by weaker antiferromagnetic exchange or, perhaps, even by ferromagnetic exchange-coupling constants.[15] For $S = 4$, these exchange interactions yield a spin state in which the spins of the three equivalent sites are aligned antiparallel to the spin of the unique site, as observed experimentally. The spin ordering for each minimum is shown in Figure 11. Thus, for the $S = 4$ state, our theoretical model correctly predicts the 3:1 ratio as well as the ordering of the iron spins, resulting from spontaneous symmetry breaking. The energies and states at the minima can be expressed analytically for any value of $S$. Let us consider the case for which $Fe_4$ is the unique site. For $J_{14} = J_{24} = J_{34} = J$ and $J_{12} = J_{13} = J_{23} = J'$, the spin Hamiltonian in eq 7 can be diagonalized by first coupling the spins of the three equivalent sites to composite spin $S_{123}$ ($\hat{\mathbf{S}}_{123} = \hat{\mathbf{S}}_1 + \hat{\mathbf{S}}_2 + \hat{\mathbf{S}}_3$), followed by a coupling of $S_{123}$ to spin $S_4$ of the unique site to give the total spin $S$. The spin quantum numbers fulfill the following triangular inequalities: $|S_1 - S_2| \le S_{12} \le S_1 + S_2$, $|S_{12} - S_3| \le S_{123} \le S_{12} + S_3$, and $|S_{123} - S_4| \le S \le S_{123} + S_4$. As an example, we have listed in Table 3 the allowed values for $S_{123}$ for $S = 4$, together with the number of multiplets for each value.

By using $J$ and $J'$ in eq 7, we obtain for the eigenstates the exchange energy

$$E(S, S_{123}) = \frac{1}{2}JS(S+1) + \frac{1}{2}(J' - J)S_{123}(S_{123}+1) - 3J - 9J' \tag{16}$$

Substitution of $J = J^\circ + \Delta J$ and $J' = J^\circ - \Delta J$ into eq 16 and the addition of the elastic energies for the six Fe−Fe pairs then yield the total energy

$$E_T(S, S_{123}, \delta J) = E^\circ(S) + \Delta E_T(S, S_{123}, \delta J) = J^\circ\left\{\frac{1}{2}S(S+1) - 12 + \left[\frac{1}{2}S(S+1) - S_{123}(S_{123}+1) + 6\right]\delta J + 6\kappa_T\,\delta J^2\right\} \tag{17}$$

Given that the $S_{123}(S_{123} + 1)$ term has a negative sign, the lowest energy is attained for the maximum value of $S_{123}$ that is allowed for the given value of $S$ ($S_{123}^{max}$; see Table 4).

The energy minimum of $E_T(S, S_{123}^{max}, \delta J)$ as a function of $\delta J$ is obtained for

$$\delta J_T^{min}(S) = -\frac{\frac{1}{2}S(S+1) - S_{123}^{max}(S_{123}^{max}+1) + 6}{12\kappa_T} \tag{18}$$

The values of the numerator of eq 18 are listed as a function of $S$ in the third column of Table 4. The corresponding minimum in $T_2$ space is located at $-\delta t_1 = -\delta t_2 = \delta t_3 = \sqrt{2}\delta J_T^{min}$. The expression for the energy at the minimum is obtained by substitution of eq 18 into eq 17

$$E_T^{min}(S) = E_T\left(S, S_{123}^{max}, \delta J_T^{min}(S)\right) = E^\circ(S) + \Delta E_T(S) \tag{19}$$

In the third part of eq 19, the energy is expressed as the sum of the exchange energy of the undistorted cluster (eq 8) and a distortion-related energy

$$\Delta E_T(S) = \Delta E_T\left(S, S_{123}^{max}, \delta J_T^{min}(S)\right) \tag{20a}$$

In units of $J^\circ$, the energy in eq 20a can be expressed as

$$\frac{\Delta E_T(S)}{J^\circ} = -\frac{2[12\kappa_T\,\delta J_T^{min}(S)]^2}{48\kappa_T} \tag{20b}$$

The values of the numerator of the energy in eq 20b are listed as a function of $S$ in the fourth column of Table 4.

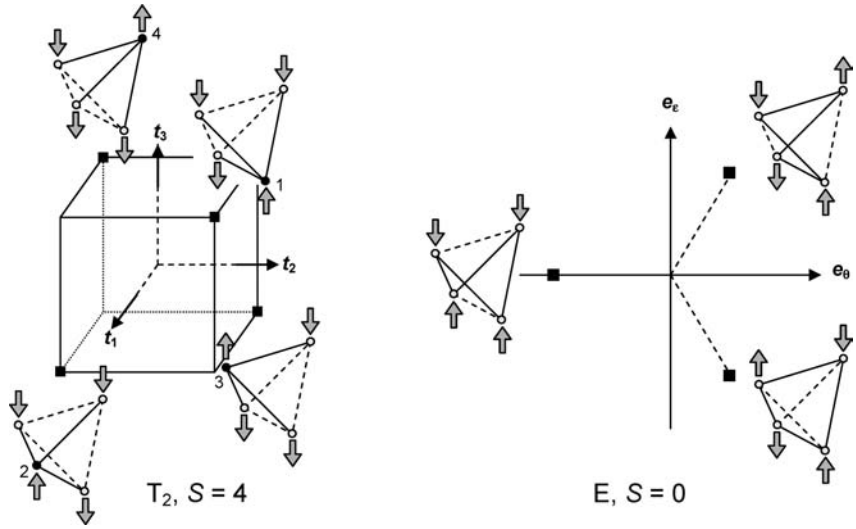


**Figure 11.** (left) Schematic representation of the positions of the four degenerate energy minima (black squares) of the potential energy surface for the cluster in the three-dimensional $T_2$ space. The cube containing the equilateral tetrahedron with the locations of the minima has been indicated. The spin ordering of the irons for $S = 4$ is shown for each minimum. The solid and dashed lines in each cartoon connect iron pairs for which the exchange interactions are increased and decreased, respectively, as a result of the distortion. The unique site for each minimum has been indicated by a filled circle. (right) Schematic representation of the positions of the three degenerate energy minima (black squares) of the potential energy surface for the cluster in the two-dimensional E space. The minima are located at the vertices of an equilateral triangle. The spin ordering of the irons for $S = 0$ has been shown for each minimum. The solid and dashed lines in each cartoon connect iron pairs in which the exchange-coupling constants are increased and decreased, respectively, as a result of the distortion.

**Table 3.** Subcluster Spins in $S = 4$ States

| $S$ | $S_{12}$ | $S_{123}$ | no. of multiplets |
|---|---|---|---|
| 4 | 0−4 | 2 | 5 |
| 4 | 1−4 | 3 | 4 |
| 4 | 2−4 | 4 | 3 |
| 4 | 3, 4 | 5 | 2 |
| 4 | 4 | 6 | 1 |

**Table 4.** Size and Energy of $T_2$ Distortion[a]

| $S$ | $S_{123}^{max}$ | $12\kappa_T\ \delta J_T^{min}(S)$ | $48\kappa_T \Delta E_T(S)/J^\circ$ |
|---|---|---|---|
| 0 | 2 | 0 | 0 |
| 1 | 3 | 5 | −50 |
| 2 | 4 | 11 | −242 |
| 3 | 5 | 18 | −648 |
| 4 | 6 | 26 | −1352 |
| 5 | 6 | 21 | −882 |
| 6 | 6 | 15 | −450 |
| 7 | 6 | 8 | −128 |
| 8 | 6 | 0 | 0 |

[a] The values listed for $S_{123}^{max}$ follow from the triangular inequalities for the coupling of $S_{123}$ ($0 \le S_{123} \le 6$) and $S_4$ to resultant spin $S$: $|S_{123} - S_4| \le S \le S_{123} + S_4$.

While $S = 0$ and 8 are $T_2$-inactive, the largest activity for this mode is found for $S = 4$, which allows this state to become the ground state (see below). In our treatment, the spin ordering of the $T_2$ minimum for $S = 4$ is a consequence of the theoretical model and is not imposed as in the pioneering broken-symmetry density functional theory (DFT) calculations for the $M_S = 4$ state of the all-ferrous cluster by Torres et al.[16] Our results differ further in that the structure of the Fe−S core is predicted to have a 3-fold axis, while this symmetry is absent in the DFT-optimized structure.

**4.3. E Distortion.** The three degenerate minima of the potential energy surface for the ground state in the E space are located at the vertices of an equilateral triangle (Figure 11, right). The symmetry of the cluster at the minima is $D_{2d}$. The six exchange-coupling constants at the E minima are partitioned into two sets. For example, $J_{13} = J_{14} = J_{23} = J_{24} = J$ and $J_{12} = J_{34} = J'$ with $J > J'$ at the minimum on the $e_\theta$ axis. The latter two coupling constants provide weaker antiferromagnetic (or ferromagnetic) interactions inside two disjoint pairs and stronger antiferromagnetic interactions between the two pairs. The Hamiltonian in eq 7 can be diagonalized analytically by first coupling the spins of the disjoint pairs to give pairs with spin $S_{12}$ and $S_{34}$ ($\hat{\mathbf{S}}_{12} = \hat{\mathbf{S}}_1 + \hat{\mathbf{S}}_2$ and $\hat{\mathbf{S}}_{34} = \hat{\mathbf{S}}_3 + \hat{\mathbf{S}}_4$), followed by a coupling of the pair spins to give resultant spin $S$. The spin quantum numbers fulfill the following triangular inequalities: $|S_1 - S_2| \le S_{12} \le S_1 + S_2$, $|S_3 - S_4| \le S_{34} \le S_3 + S_4$, and $|S_{12} - S_{34}| \le S \le S_{12} + S_{34}$. The energies of the eigenstates of eq 7 can be written as

$$E(S, S_{12}, S_{34}) = \frac{1}{2}JS(S+1) + \frac{1}{2}(J' - J)\{S_{12}(S_{12}+1) + S_{34}(S_{34}+1)\} - 12J' \quad (21)$$

Substitution of $J = J^\circ + (1/2)\Delta J$ and $J' = J^\circ - \Delta J$ into eq 21 and the addition of the elastic energies for the six Fe−Fe pairs give for the total energy the expression

$$E_E(S, S_{12}, S_{34}, \delta J) = E^\circ(S) + \Delta E_E(S, S_{12}, S_{34}, \delta J) = J^\circ\left\{\frac{1}{2}S(S+1) - 12 + \left[\frac{1}{4}S(S+1) - \frac{3}{4}\{S_{12}(S_{12}+1) + S_{34}(S_{34}+1)\} + 12\right]\delta J + 3\kappa_E\,\delta J^2\right\} \quad (22a)$$

For any value of $S$, the lowest energy is obtained for the maximum value of the intermediate spins, $S_{12} = S_{34} = 4$. Substitution of these values into eq 22a yields eq 22b

$$E_E(S, \delta J) = E^\circ(S) + \Delta E_E(S, \delta J) = J^\circ\left\{\frac{1}{2}S(S+1) - 12 + \left[\frac{1}{4}S(S+1) - 18\right]\delta J + 3\kappa_E\,\delta J^2\right\} \quad (22b)$$

The energy minimum of $E_E(S, \delta J)$ is obtained at

$$\delta J_{\mathrm{E}}^{\min}(S) = \frac{36 - \frac{1}{2}S(S+1)}{12\kappa_{\mathrm{E}}} \tag{23}$$

The corresponding minimum in the E space is located at $\delta e_\theta = -\sqrt{3}\delta J_{\mathrm{E}}^{\min}$ and $\delta e_\varepsilon = 0$. The expression for the energy at the minimum is obtained by substitution of eq 23 into eq 22b

$$E_{\mathrm{E}}^{\min}(S) = E_{\mathrm{E}}\left(S, \delta J_{\mathrm{E}}^{\min}(S)\right) = \mathrm{E}^\circ(S) + \Delta E_{\mathrm{E}}(S) \tag{24}$$

where we have used the definition

$$\Delta E_{\mathrm{E}}(S) = \Delta E_{\mathrm{E}}\left(S, \delta J_{\mathrm{E}}^{\min}(S)\right) \tag{25a}$$

In units of $J^\circ$, the energy in eq 25a can be expressed as

$$\frac{\Delta E_{\mathrm{E}}(S)}{J^\circ} = -\frac{[12\kappa_{\mathrm{E}}\,\delta J_{\mathrm{E}}^{\min}(S)]^2}{48\kappa_{\mathrm{E}}} \tag{25b}$$

The values of the numerators of eqs 23 and 25b have been listed as a function of $S$ in Table 5. The E activity is largest for $S = 0$, decreases with increasing values of the spin, and eventually vanishes for $S = 8$. A comparison of Tables 4 and 5 shows that $\kappa_{\mathrm{T}}\,\delta J_{\mathrm{T}}^{\min}(S) = \kappa_{\mathrm{E}}\,\delta J_{\mathrm{E}}^{\min}(S)$ and $\kappa_{\mathrm{T}}\Delta E_{\mathrm{T}}(S) = 2\kappa_{\mathrm{E}}\Delta E_{\mathrm{E}}(S)$ for $S > 3$.

**4.4. Relative Energies of Minima.** In this section, we analyze the relative energies of the $T_2$ and E minima for the nine spin states of the all-ferrous cluster.[17] In particular, we present for each value of $S$ the condition for which the $T_2$ minimum is below the E minimum, the conditions for the level crossings between the $T_2$ minimum for $S = 4$ and the $T_2$ minima for $S < 4$, and finally the condition for which the $T_2$ minimum for $S = 4$ is the absolute minimum.

The $T_2$ minimum for spin $S$ is lower in energy than the E minimum for the same value of the spin provided $|\Delta E_{\mathrm{T}}(S)| > |\Delta E_{\mathrm{E}}(S)|$. The inequality implies that the force constants for $T_2$ and E satisfy the condition $\kappa_{\mathrm{T}}/\kappa_{\mathrm{E}} < q_S$, with $q_S$ being the value given in Table 6. Because $S = 0$ is $T_2$-inactive, the E minimum is lowest for any finite value of $\kappa_{\mathrm{E}}$. For $S = 1-4$, the condition is fulfilled for increasingly larger values for $\kappa_{\mathrm{T}}/\kappa_{\mathrm{E}}$. (N.B. In general, a large force constant implies a small distortion (energy). Thus, a higher $q_S$ value signifies an increased propensity for the $T_2$ minimum to be lowest.).

Above we mentioned that the largest $T_2$ stabilization energy, $|\Delta E_{\mathrm{T}}(S)|$, is attained for $S = 4$ (Table 4). In the limit $\kappa_{\mathrm{T}} \rightarrow \infty$, where the distortion energies vanish for all values of $S$, the $S = 4$ energy is greater than the energies for $S = 0-3$ (eq 8). When the value for $\kappa_{\mathrm{T}}$ is lowered, the energy of the $T_2$ minimum for $S = 4$ drops relative to those for the other spin states and consecutively crosses the energies of the $T_2$ minima for $S = 3$, 2, 1, and 0 at the values $\kappa_{\mathrm{T}} = p_S$ listed in Table 7. We note that the $p_S$ values are an increasing function of $S$. Thus, if the condition for the crossing with $S = 0$ ($\kappa_{\mathrm{T}} < 2.817$; Table 7) is fulfilled, then the $T_2$ minimum for $S = 4$ has the lowest energy of all $T_2$ minima. The crossing with $S = 0$ considered here is with an undistorted level because $S = 0$ is $T_2$-inactive (Table 4).

Because the exchange energy of the unperturbed cluster, $E^\circ(S)$, and the E stabilization energy, $|\Delta E_{\mathrm{E}}(S)|$, are increasing and decreasing functions of spin quantum number $S$, respectively (Tables 2 and 5), the energy at the E minima, $E_{\mathrm{E}}^{\min}(S)$, is an increasing function of $S$. Thus, the E minimum for $S = 0$ is among the E minima the lowest in energy for any value for $\kappa_{\mathrm{E}}$. Hence, the $T_2$ minimum for $S = 4$ is lower in energy than any of the E minima, provided $E_{\mathrm{T}}^{\min}(S = 4) < E_{\mathrm{E}}^{\min}(S = 0)$. The latter condition implies an inequality for the ratio of the force constants for the T and E distortions,

$$\frac{\kappa_{\mathrm{T}}}{\kappa_{\mathrm{E}}} < \frac{169 - 60\kappa_{\mathrm{T}}}{162} \tag{26}$$

In the limit $\kappa_{\mathrm{E}} \rightarrow \infty$ (where the E distortion for $S = 0$ vanishes), the condition reduces to the condition $\kappa_{\mathrm{T}} < p_{S=0}$, which ascertains that the $T_2$ minimum for $S = 4$ is lower in energy than the one for $S = 0$ (Table 7). Having established that the $T_2$ minimum for $S = 4$ is lower in energy than (i) all E minima and (ii) all $T_2$ minima for $S \neq 4$, it follows that eq 26 is the condition that ensures that the $T_2$ minimum for $S = 4$ is the absolute energy minimum of the all-ferrous cluster. Finally, it can be shown that if the absolute minimum is a $T_2$ minimum, then it must be the $T_2$ minimum for $S = 4$. Thus, the absolute minimum is either the $T_2$ minimum for $S = 4$ or the E minimum for $S = 0$. The latter minimum is the absolute minimum if the condition in eq 26 is violated. The origin of the differences in the force constants required for the stabilization of the $T_2$ minimum is the subject of a separate study.

The conditions described in this section have a number of corollaries:

(a) The largest value of $\kappa_{\mathrm{T}}/\kappa_{\mathrm{E}}$ for which the $T_2$ minimum for $S = 4$ is the ground state is $^{169}/_{162} \approx 1.04$. Thus, $\kappa_{\mathrm{T}}$ must

**Table 5.** Size and Energy of E Distortion

| $S$ | $12\kappa_{\mathrm{E}}\,\delta J_{\mathrm{E}}^{\min}(S)$ | $48\kappa_{\mathrm{E}}\Delta E_{\mathrm{E}}(S)/J^\circ$ |
|---|---|---|
| 0 | 36 | −1296 |
| 1 | 35 | −1225 |
| 2 | 33 | −1089 |
| 3 | 30 | −900 |
| 4 | 26 | −676 |
| 5 | 21 | −441 |
| 6 | 15 | −225 |
| 7 | 8 | −64 |
| 8 | 0 | 0 |

**Table 6.** Condition $\kappa_{\mathrm{T}}/\kappa_{\mathrm{E}} < q_S$ for Which the $T_2$ Minimum Is below the E Minimum for Given Values of $S$

| $S$ | $q_S$ | |
|---|---|---|
| 0 | 0 | 0.000[a] |
| 1 | $^2/_{49}$ | 0.041[b] |
| 2 | $^2/_9$ | 0.222 |
| 3 | $^{18}/_{25}$ | 0.720 |
| 4−7 | 2 | 2.000 |
| 8 | [c] | |

[a] The E minimum is below the $T_2$ minimum for any positive value of $\kappa_{\mathrm{E}}$. [b] Decimal representation of the ratio. [c] Jahn−Teller-inactive in both $T_2$ and E spaces.

**Table 7.** Conditions $\kappa_{\mathrm{T}} < p_S$ for Which the $T_2$ Minimum for $S = 4$ Is Lower in Energy Than the $T_2$ Minimum for $S = 0-3$

| $S$ | $p_S$ | |
|---|---|---|
| 0 | $^{169}/_{60}$ | 2.817[a] |
| 1 | $^{217}/_{72}$ | 3.014 |
| 2 | $^{185}/_{56}$ | 3.304 |
| 3 | $^{11}/_3$ | 3.666 |

[a] Decimal representation of the ratio.

typically be smaller than $\kappa_E$ ($\kappa_E \approx 1.04\kappa_E > \kappa_T$) to obtain an $S = 4$ ground state. Thus, under this condition, the electronic state at the absolute energy minima is similar to the "3:1", $S = 4$ state inferred from spectroscopic analysis of the all-ferrous clusters in complex **1** and *Av*2.

(b) For $\kappa_T/\kappa_E = 1$, eq 26 implies $\kappa_T < {}^{7}/_{60}$ and $\Delta J > {}^{130}/_{7}$ $J°$. Thus, in the case of equal force constants, the force constant for $T_2$ must be small and the change in $J$ very large in order to obtain an $S = 4$ ground state.

(c) To obtain a $T_2$ minimum for $S = 4$ with vanishing coupling constants between the three equivalent sites ($J' = 0$) requires that $\delta J_T^{min}(S = 4) = 1$. This condition and the expression $\kappa_T\, \delta J_T^{min}(S = 4) = {}^{13}/_{6}$ (Table 4) yield the value $\kappa_T = {}^{13}/_{6} \approx 2.167$. Substitution in eq 26 yields the condition $\kappa_E > 9$ for ensuring that the $T_2$ minimum for $S = 4$ is the absolute minimum. For $J' > 0$ ($J'$ antiferromagnetic), the $T_2$ minimum for $S = 4$ is the absolute minimum if ${}^{13}/_{6} < \kappa_T < {}^{169}/_{60}$ and $\kappa_E > \kappa_E^{lim} = 162\kappa_T/(169 - 60\kappa_T)$; the limiting value for $\kappa_E$ varies as a function of $\kappa_T$ in the range $9 < \kappa_E^{lim} < \infty$. For $J' < 0$ ($J'$ ferromagnetic), the $T_2$ minimum for $S = 4$ is the absolute minimum if $\kappa_T < {}^{13}/_{6}$ and $\kappa_E > \kappa_E^{lim}$; the limiting value for $\kappa_E$ varies as a function of $\kappa_T$ in the range $0 < \kappa_E^{lim} < 9$.

(d) The upper limit of $\kappa_T$ (${}^{169}/_{60}$; eq 26) and the lower limit of $\delta J_T^{min}(S = 4)$ (${}^{13}/_{6}/\kappa_T = {}^{10}/_{13}$) for which the $T_2$ minimum for $S = 4$ remains the absolute minimum are reached in the limiting case $\kappa_E \rightarrow \infty$. For these values, we obtain the largest possible value for $J' = J°[1 - \delta J_T^{min}(S = 4)] = {}^{3}/_{13}J° \approx 0.231J°$ consistent with an absolute $T_2$ minimum of $S = 4$. In this limit, we find that $J = J°[1 + \delta J_T^{min}(S = 4)] = {}^{23}/_{13}J° \approx 1.769J°$ and $J'/J = {}^{3}/_{23} \approx 0.13$. Smaller values for the $J'/J$ ratio, including negative values arising from ferromagnetic $J'$ values, are found away from the limit.

## 5. Application of the Theoretical Model to All-Ferrous Clusters

**5.1. Unique Sites in the All-Ferrous Clusters of Complex 1 and Iron Protein.** Given certain core-specific conditions on the force constants, we identified in the previous section a "3:1", $S = 4$ state as the ground state of the all-ferrous cluster on the basis of a theoretical analysis that completely ignores external perturbations and exclusively focuses on the $[Fe_4S_4]^0$ core. The intrinsic (core-specific) nature of this solution suggests why the same ground state is present in both complex **1** and the protein-bound all-ferrous cluster of *Av*2, in spite of significant differences in their terminal coordination. Thus, the present study strongly suggests that the "3:1", $S = 4$ ground state of the all-ferrous *Av*2 cluster is not imposed on the cluster by changes in the exchange-coupling constants induced by the protein environment, as suggested in an earlier study,[8] but is an intrinsic property of the cluster core. The magnetostructural correlation between $J$ and the metal−ligand−metal angle, notably the increase in the value for $J$ as a function of this angle, frequently observed in a series of structurally related transition-metal complexes,[15] suggests that the antiferromagnetic couplings in the Fe−S−Fe bridges of the all-ferrous cluster become larger when the bond angles are increased. Thus, we predict that the angles $Fe_i$−$S_k$−$Fe_j$ for $i = 1-3$ and $j = 4$ (i.e., for bridges between one of the equivalent sites and the unique site) are larger than those for $i, j = 1-3$ (i.e., for bridges between the three equivalent iron sites). The prediction is confirmed by the data for these angles listed in Table 8. Indeed, in both the protein-bound cluster and complex **1**, the former angles are >70° with an average of 71.9° and the latter angles are <70° with an average of 67.8°. The remarkable agreement in the angular values for the two clusters (see Table 8) corroborates the intrinsic (core-based) nature of the forces shaping the core conformation. In the labeling adopted in Table 8, the unique site is designated as $Fe_4$ both in complex **1** and in the all-ferrous cluster of the iron protein. The unique site ($Fe_4$ in our numbering) appears in PDB file 1G1M,[7] containing the structure of the all-ferrous iron protein of *A. vinelandii*, as iron site Fe(3), which is one of the two solvent-exposed irons of the cluster. A complete correspondence list is given in footnote b of Table 8. The Fe−Fe distances show the same trend as the bond angles (see Table S2 in the Supporting Information), with the $Fe_4$−$Fe_i$ ($i = 1-3$) distances being on average 0.15/0.10 Å (iron protein/complex **1**) longer than the $Fe_i$−$Fe_j$ ($i, j = 1-3$) distances. Concomitantly, the diagonal distances for the unique sites, $Fe_4$−$S_4$ = 4.090/4.059 Å (iron protein/complex **1**) are 0.24/0.17 Å longer than the $Fe_i$−$S_i$ ($i = 1-3$) distances for the three equivalent sites $\langle Fe_i\text{−}S_i\rangle_{avg}$ = 3.853/3.866 Å. Thus, we have succeeded in assigning the unique *spectroscopic* iron site, identified in the all-ferrous iron protein by Yoo et al.,[6] to a specific *structural* site in the crystallographic structure of the cluster (Figure 12). Similarly, we have identified the unique site in the Mössbauer spectra of complex **1** (Figures 3 and 5) to site $Fe_4$ in its structure (Figure 1).

**Table 8.** Fe−S−Fe Bond Angles in All-Ferrous Clusters in *Av*2 and Complex **1**

| | $Fe_i$−$S_k$−$Fe_j$ (deg)[a,b] | |
|---|---|---|
| *i*, *k*, *j* | protein | complex **1** |
| 1, 2, 4 | 74.0 | 71.9 |
| 1, 3, 4 | 73.7 | 71.2 |
| 2, 1, 4 | 70.8 | 71.2 |
| 2, 3, 4 | 70.5 | 71.3 |
| 3, 1, 4 | 70.7 | 73.2 |
| 3, 2, 4 | 70.7 | 73.4 |
| av. | **71.7** | **72.0** |
| 1, 3, 2 | 66.8 | 68.0 |
| 1, 4, 2 | 66.9 | 67.3 |
| 1, 2, 3 | 69.9 | 69.8 |
| 1, 4, 3 | 68.5 | 70.0 |
| 2, 1, 3 | 65.7 | 68.0 |
| 2, 4, 3 | 64.5 | 67.5 |
| av. | **67.1** | **68.4** |

[a] The sulfur atoms carry the same labels as the diagonally opposite irons (Figure 8). [b] The sites here labeled $Fe_1$, $Fe_2$, $Fe_3$, and $Fe_4$ correspond with Fe(1), Fe(4), Fe(2), and Fe(3) in the PDB file 1G1M containing the structure of the all-ferrous iron protein of *A. vinelandii* and with Fe(1), Fe(3), Fe(4), and Fe(2) of complex **1** in the labeling of ref 2, respectively.

The unique sites in the all-ferrous clusters of complex **1** and iron protein can also be identified by comparing the cluster cores in these systems. Table 9 presents a list containing all 12 possible overlays of the two cluster cores together with the resulting root-mean-square deviations (RMSDs) for iron-only as well as 4Fe−4S-based minimizations. Using our atom labeling, mappings that assign site $Fe_4$

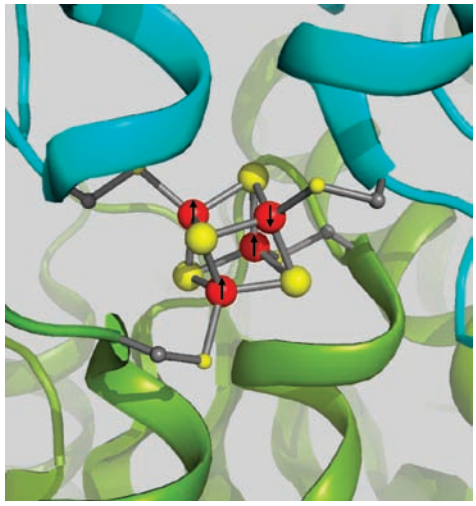

**Figure 12.** Segment of the all-ferrous iron protein (PDB code 1G1M) viewed from the solvent-exposed face of the $[Fe_4S_4]^0$ cluster. Color code: subunit A, blue ribbon; subunit B, green ribbon; irons, red spheres; sulfurs, yellow spheres. The front iron atom connected to subunit A is labeled Fe(3) in the PDB file and $Fe_4$ in our discussion and is the iron site that has been identified as the unique spectroscopic site of the cluster in this work. The front iron atom connected to subunit B is labeled Fe(1) in the PDB file and $Fe_1$ in our discussion. The ordering of the iron spins in the $S = 4$ state of the all-ferrous cluster is indicated by arrows; the arrow at the unique site points downward; the arrows of the "equivalent" sites point upward.

**Table 9.** RMSDs for the 12 Overlays of the All-Ferrous Clusters in *Av*2 and Complex **1**

| case | mapping | RMSD 4Fe (Å) | RMSD 4Fe−4S (Å) |
|---|---|---|---|
| 1 | 1, 2, 3, 4[a] | **0.053** | **0.060** |
| 2 | 2, 3, 1, 4 | **0.071** | **0.070** |
| 3 | 3, 1, 2, 4 | **0.050** | **0.066** |
| 4 | 2, 4, 3, 1 | 0.121 | 0.127 |
| 5 | 4, 1, 3, 2 | 0.099 | 0.096 |
| 6 | 3, 2, 4, 1 | 0.095 | 0.094 |
| 7 | 4, 2, 1, 3 | 0.068 | 0.081 |
| 8 | 1, 3, 4, 2 | 0.121 | 0.127 |
| 9 | 1, 4, 2, 3 | 0.103 | 0.102 |
| 10 | 3, 4, 1, 2 | 0.122 | 0.122 |
| 11 | 4, 3, 2, 1 | 0.089 | 0.090 |
| 12 | 2, 1, 4, 3 | 0.102 | 0.105 |

[a] Mapping of iron sites in the all-ferrous cluster in *Av*2 to those of the all-ferrous cluster in complex **1**. For example, in case 2, $Fe_1 \rightarrow Fe_2$, $Fe_2 \rightarrow Fe_3$, $Fe_3 \rightarrow Fe_1$, and $Fe_4 \rightarrow Fe_4$ (*Av*2 → complex **1**).

of the iron protein cluster to site $Fe_4$ of complex **1** give consistently the lowest three RMSDs (indicated in boldface), confirming that $Fe_4$ is the unique site in both systems. Accordingly, interchanges of the equivalent sites, $Fe_1$, $Fe_2$, and $Fe_3$, obtained by applying the pseudo-$C_3$ symmetry operator, produce only minor changes in the RMSDs. The first overlay of Table 9 (case 1) is shown in Figure 13 and reveals a remarkable degree of congruence between the two cluster cores. Given the rather low resolution (2.25 Å) of the all-ferrous iron protein structure, it may seem unlikely that it is feasible to identify the unique site in the X-ray structure. However, it should be noted that the Debye−Waller factors of the core atoms are about half the protein average, implying that the core structure is much better defined than the overall protein structure. Strop et al.[7] concluded from the low Debye−Waller factors that the crystallographic cluster structure pertains to a single conformation, as is implicitly assumed in our analysis, and not to a conformational superposition. In this respect, not surprisingly, the

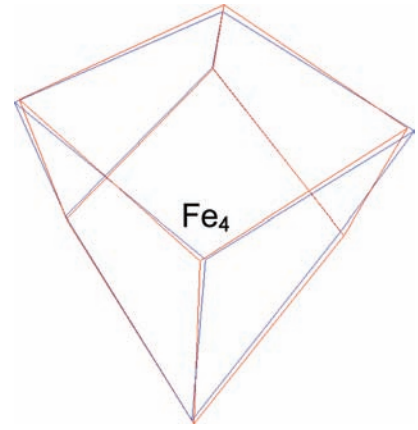


**Figure 13.** Overlay of the all-ferrous Fe−S core in complex **1** (red) and that in the iron protein of *A. vinelandii* (blue). The overlay is obtained by minimizing the RMSD between the corresponding iron and sulfur atoms of the two cores for the site-to-site mapping defined in case 1 of Table 9. Case 1 is one of the three mappings that map the unique sites (labeled $Fe_4$) of the two cores onto each other and give significantly lower RMSDs.

protein environment cannot be entirely dismissed because it apparently locks the cluster core into one of its intrinsic minima.

**5.2. Is There Experimental Evidence for E, $S = 0$ Minima in All-Ferrous Clusters?** The spectroscopic and structural evidence discussed so far support the presence of $T_2$, $S = 4$ minima in the all-ferrous clusters of two systems, viz., complex **1** and the iron protein from *A. vinelandii*. Some literature data raise the possibility that all-ferrous clusters may also appear in the alternative E, $S = 0$ minima. In a report of an extended X-ray absorption fine structure (EXAFS) study of the titanium(III) citrate-reduced all-ferrous cluster in the iron protein of *A. vinelandii*, the Fe−Fe distances appear in two sets, one consisting of two long distances and the other of four short distances.[18] These distances are consistent with the $D_{2d}$ symmetry of the E minima. However, such an assignment appears to be baseless taking into consideration the following points: (1) Mössbauer studies of titanium(III) citrate-reduced iron protein unambiguously show that the all-ferrous cluster has an $S = 4$ ground state rather than the $S = 0$ state predicted for the E minimum. (2) Given the magnetostructural correlation between the exchange-coupling constant and bridging angle, the E minimum is predicted to have a cluster structure with two short and four long Fe−Fe distances rather than two long and four short distances as inferred from the EXAFS data. (3) The analysis described in the EXAFS report assumes that all iron sites are equivalent, precluding the identification of core conformations with inequivalent sites, such as the $C_{3v}$-symmetric $T_2$ conformation. (4) A reversal in the energy order of the $T_2$ and E minima would require significant changes in the force constants for these, otherwise remarkably conserved (Figure 13), core units. In a recent EPR and magnetic susceptibility study of flavodoxin hydroquinone ($E_m$

(16) Torres, R. A.; Lovell, T.; Noodleman, L.; Case, D. A. *J. Am. Chem. Soc.* **2003**, *125*, 1923–1936.
(17) The force constant $\kappa_A$ for the symmetric mode is assumed to be ∞.
(18) Musgrave, K. B.; Angove, H. C.; Burgess, B. K.; Hedman, B.; Hodgson, K. O. *J. Am. Chem. Soc.* **1998**, *120*, 5325–5326.

= −515 mV) treated *Av*2, the Fe−S cluster was reported to be in an all-ferrous, $S = 0$ state.[9] This claim, however, has not yet been substantiated by application of a technique sensitive to the oxidation state of the cluster and should, given point 4 and the high potential at which the state was generated, be viewed with caution.

**5.3. Graphical Comparison of Cores in Complex 1 and *Av*2.** In Figure S2A,B in the Supporting Information, we have presented graphical comparisons of the Fe−Fe distances (Table S2 in the Supporting Information) and Fe−S−Fe angles (Table 8) of the all-ferrous cores in **1** and *Av*2. In section 5.1, it was shown that the 12 Fe−S−Fe bridge angles can be cast in two sets: a set of six small angles for bridges between the equivalent irons (set 1) and a set of six large angles for bridges between the unique site and the equivalent sites. Accordingly, the six Fe−Fe distances can be cast into sets of three short distances (set 1) and three long distances (set 2). While the angles or distances belonging to one set are predicted by our model to be equal, examination of Table S2 in the Supporting Information and Table 8 reveals that the sets contain different values. The widths of the dispersion ranges for each set can be gleaned from Figures S2A (and Figure S2B) in the Supporting Information: for set 1, the widths are 0.07 Å (2.7°) in complex **1** and 0.11 Å (5.4°) in *Av*2; for set 2, the spreads are 0.05 Å (2.2°) in complex **1** and 0.12 Å (3.3°) in *Av*2. The averages for the sets have been indicated by dashed arrows in the figures and are separated by 0.10 Å (3.6°) in complex **1** and by somewhat higher values, 0.15 Å (4.6°), in *Av*2. The set widths are smaller than the separations between the set averages in complex **1** and of similar magnitude in *Av*2. Interestingly, the two clusters exhibit the same correlation between the distances of the two sets: the shortest distance of set 1 ($Fe_1-Fe_2$ in **1** and $Fe_2-Fe_3$ in *Av*2) and the longest distance of set 2 ($Fe_3-Fe_4$ in **1** and $Fe_1-Fe_4$ in *Av*2) belong to complementary iron pairs; analogously, the intermediate distance of set 1 ($Fe_2-Fe_3$ in **1** and $Fe_1-Fe_2$ in *Av*2) and the intermediate distance of set 2 ($Fe_1-Fe_4$ in **1** and $Fe_3-Fe_4$ in *Av*2) and the longest distance of set 1 ($Fe_1-Fe_3$ in **1** and $Fe_1-Fe_3$ in *Av*2) and the shortest distance of set 2 ($Fe_2-Fe_4$ in **1** and $Fe_2-Fe_4$ in *Av*2) belong to complementary pairs as well. A similar correlation exists for Fe−S−Fe angles. In terms of symmetrized coordinates, the correlation indicates that the core structures of the two clusters are predominantly distorted in $T_2$ space. However, because the three complementary pairs of Fe−Fe distances are separated by different distances, the cluster locations in $T_2$ space are displaced with respect to the diagonal positions of the $T_2$ minima shown in Figure 11 (left). The qualitative similarity of the distortions in **1** and *Av*2 suggests that it is an intrinsic property of the core unit, although the amplitudes of the distortions differ between the two clusters, implying that the intrinsic distortional forces have been modulated by the changes in the terminal ligation or cluster environment. We anticipate that a full understanding of these distortions will require an extension of the model presented in this paper by taking explicitly the 3d orbital states of the irons and their relationship to the exchange interactions between the irons into consideration. The distortions are partly reproduced by the DFT calculations for the broken-symmetry configuration representing the $S = 4$ state of *Av*2 by Torres et al.,[16] who obtained a layered structure in which the six Fe−Fe distances appear as one short distance, four equal intermediate distances, and one long distance, with the short and long distances connecting complementary iron pairs and the unique site belonging to the long-distance pair. Thus, the structure obtained by Torres et al. shows also a distortion in $T_2$ space but one that, unlike the $T_2$ minima of Figure 11, is located on a $t_i$ axis. This prediction differs from the X-ray data for both **1** and *Av*2 in that the four intermediate Fe−Fe distances are equal and not dispersed over ranges with widths of ∼0.1 Å as in the X-ray structures. Torres et al. reported also DFT calculations for the broken-symmetry configuration representing the $S = 0$ state and found that, while this state is lower in energy than the broken-symmetry $S = 4$ state in the gas phase, the "$S = 4$" state becomes lowest by a wide margin of ∼2000 $cm^{-1}$ when the cluster is placed in a protein/solvent-simulating environment, suggesting an essential role of the protein in the stabilization of the $S = 4$ state. In contrast, our analysis of complex **1** shows that the $S = 4$ ground state of the all-ferrous core is also accessible in the absence of a hydrogen-bonding protein/water environment, adding support to the idea that the $S = 4$ ground state is an intrinsic property of the core.

**Acknowledgment.** This research was supported by NSF Grant MCB 0424494 to E.M. and NIH Grant GM 28856 to R.H.H.

**Supporting Information Available:** Ranges of the Mössbauer parameters for the complex **1** (Table S1), Fe−Fe distances in the all-ferrous clusters of *Av*2 and complex **1** (Table S2), spin expectation values for the lowest state of an $S = 4$ multiplet (Figure S1), graphical comparison of the Fe−Fe distances in the all-ferrous clusters of complex **1** and *Av*2 (Figure S2A), and graphical comparison of Fe−S−Fe angles in the all-ferrous clusters of complex **1** and *Av*2 (Figure S2B). This material is available free of charge via the Internet at http://pubs.acs.org.

IC802192W